Journal of Catalysis 263 (2009) 380–389

Contents lists available at ScienceDirect

Journal of Catalysis

www.elsevier.com/locate/jcat

# A DFT study on the removal of adsorbed sulfur from a nickel(111) surface: Reducing anode poisoning

Natasha M. Galea, John M.H. Lo *, Tom Ziegler

*Department of Chemistry, University of Calgary, 2500 University Drive, Calgary, Alberta T2N 1N4, Canada*

ARTICLE INFO

*Article history:*
Received 29 October 2008
Revised 5 February 2009
Accepted 2 March 2009
Available online 24 March 2009

*Keywords:*
Elemental sulfur
Oxygen
Sulfur dioxide
Solid-oxide fuel cell
Anode deactivation
Post-treatment
Sulfur poisoning

ABSTRACT

This report presents the results of our studies on the second step of the post-treatment of the solid-oxide fuel cells (SOFCs) that have been poisoned by sulfur from traces of $H_2S$ in the fuel. The removal of strongly adsorbed atomic sulfur from a planar Ni(111) surface at 0.25 ML coverage is investigated in order to explore possible ways to regain the activity of SOFCs poisoned by sulfur deposition on the anode. The predominant reaction pathway studied consists of the adsorption and dissociation of molecular oxygen, followed by the formation and desorption of sulfur dioxide. Using periodic DFT calculations, preferred adsorption sites, energies, transition states and kinetic barriers are calculated for the resulting intermediate and product species, $^*SO_x$ ($x = 0$–2) and $^*O$. Generally, concurring with the limited experimental data available at temperature >750 K, our research illustrates the considerable exergonic nature that describes the formation and desorption of $SO_2$, and shows that the removal of the remaining 25% of sulfur after the first step of post-treatment of the fuel cell can be accomplished by means of high-temperature oxidation.



## 1. Introduction

The adsorption of sulfur-based species found within hydrocarbon fuels have been known to cause the degradation of the solid-oxide fuel cell [1–3] (SOFC) anodes, in particular those made up of a nickel-composite (such as nickel–yttria-stabilized zirconia, Ni-YSZ), by blocking the adsorption sites on the anode surfaces, thus reducing the overall SOFC electrochemical activity. Hydrogen sulfide ($H_2S$) is among the most prominent S-pollutants because it readily adsorbs on a Ni surface, generating strongly bound atomic S and releasing molecular hydrogen gas ($H_2$) [4,5]. Therefore, sulfur poisoning imposes a serious problem in using SOFC with commonly available hydrocarbon fuels, which usually contain rather high levels of $H_2S$ (~5 ppm).

Technically this problem can be partly alleviated by performing pre-desulfurization reactions to purify hydrocarbon fuels before they are used within the SOFC; this process, however, is complex and not cost effective. Alternatively, the sulfur poisoning of the SOFC anode can be significantly reduced by choosing the anode material which is less reactive toward the $H_2S$ dissociative adsorption. In this perspective, extensive research has been devoted to investigating S-containing anode materials such as $CuFe_2S_4$ and $CuCo_2S_4$ [6], pervoskite-type $ABO_3$ conductors (example Refs. [7–10]) and Cu–ceria compounds [2,11].

Despite a better sulfur-tolerance and reduced coke formation, these newly tested materials are still less favorable than the traditional Ni-YSZ anodes in terms of thermal stability and facile fabrication. It is therefore desirable to gain a better understanding of the mechanism of the reactions between sulfur-containing contaminants, especially $H_2S$ in hydrocarbon fuels and Ni, which may benefit the further exploration of the development of highly sulfur-tolerant Ni-YSZ-based SOFC anodes.

Efforts have recently been devoted to experimentally probing the adverse influences of $H_2S$ on the electrochemical behaviors of Ni-based SOFC anodes [5,12–21]. It is observed that exposing the Ni-based anode to a minute amount of $H_2S$ initially induces a dramatic, yet recoverable, drop in the cell voltage, which is then gradually saturated with time, and the cell degradation becomes irreversible [16,17]. Xia and Birss attributed the recoverable sulfur-poisoning to the formation of a sulfur monolayer on the Ni anode surface that blocks the active sites for the fuel adsorption [14]. This proposition agrees with the observations from the LEED studies of Ku and Overbury [22] and the recent DFT calculations by Galea et al. [23] according to which the adsorbed sulfur atoms form an organized $p(2 \times 2)$ monolayer on Ni(111) for surface coverage below 0.25 ML. At higher surface coverage, it is proposed that sulfur atoms may either aggregate to form localized sulfur islands or penetrate into the Ni bulk to trigger the transformations into various forms of nickel sulfide, accounting for the irreversible

* Corresponding author.
*E-mail address:* jlo@ucalgary.ca (J.M.H. Lo).

0021-9517/$ – see front matter 
doi:10.1016/j.jcat.2009.03.001

SOFC cell deactivation by $H_2S$. The latter case has recently been observed experimentally by means of *in situ* Raman microspectroscopy [18].

Various chemical reagents have been tested in the regeneration process of the poisoned Ni-YSZ SOFC anode. The removal of adsorbed sulfur using $H_2$ is the reverse process of the highly exothermic dissociative adsorption of $H_2S$. The $H_2$ treatment can effectively reduce sulfur coverage down to 0.25 ML where sulfur appears as a monolayer on nickel [14]. On the other hand, the complete sulfur removal may be accomplished with $O_2$ oxidizing sulfur to gaseous $SO_2$ [24–26], although over exposure may lead to the oxidization of the Ni anode causing an irreversible damage of the cell. Large-scale first-principle DFT calculations with thermodynamic corrections concerning the surface regeneration of the sulfur-poisoned Ni(100) SOFC surface have recently been performed by Wang and Liu [20]; their results also support the conclusion that $O_2$ is an effective oxidizing agent for removing surface sulfur. Based on these observations, it is believed that the regeneration of clean Ni(111) anode surfaces is viable through a two-step treatment: (1) addition of $H_2$ that reduces the sulfur coverage from 0.50 ML to 0.25 ML; (2) oxidation with $O_2$ to remove the remaining sulfur adatoms.

Accordingly, in this work we considered the removal of atomic sulfur on Ni(111) by means of oxygen. In particular, we investigated the adsorption and dissociation of $O_2$, and the subsequent reactions with surface sulfur at 0.25 ML surface coverage leading to the formation and liberation of $SO_2$. Furthermore, we explored the possibility of surface regeneration via recombination of sulfur yielding $S_2$ with and without the proximity of adsorbed $O_2$. The emphasis here is on the reaction of $O_2$ with a Ni(111) surface holding a 25% sulfur coverage during the second stage of the post-treatment of the SOFCs.

## 2. Computational methods

### 2.1. Methodology for DFT calculations

Density functional theory (DFT) calculations were performed using the Vienna Ab initio Software Package [27–29] (VASP), with plane-wave projector augmented wave [30,31] (PAW) potentials. All calculations were spin-polarized and conducted within the generalized gradient approximation (GGA) with the PBE exchange correlation functional [32]. Each supercell slab consisted of three layers with the surface represented by a $(2 \times 2)$ unit cell. Our calculations show that replacing the three-layer slab by a four-layer slab only changes the resulting adsorption energies by a few kcal/mol while the relative stability of species is not affected. The (wave-function) kinetic energy cutoff was set to 400 eV and the (augmentation) charge density cutoff was set to 800 eV. k-Point sets were generated using the Monkhorst–Pack [33] method. All calculations made use of $5 \times 5 \times 1$ k-points in an orthorhombic unit cell. For geometry optimization searches within each reaction step all metal atoms were fixed in the slab geometries at their bulk-truncated positions in an fcc lattice with a theoretical equilibrium bulk lattice constant of $a_0 = 3.52$ Å. It should be noted that the theoretically calculated and experimentally determined bulk lattice constant ($a_0$) are nearly identical [34]. Once the optimum geometry was determined for each reaction step, coordinates were re-optimized while relaxing the top nickel surface layer to calculate more accurate minima energy. Geometries were optimized until the energy had converged to $10^{-3}$ eV. Slabs were separated in the direction perpendicular to the surface by a vacuum region of ~10 Å in order to minimize the interaction between the induced dipoles of two slabs due to the adsorption of surface species. All transition states and reaction barriers were calculated with the nudged-elastic band (NEB) method [35]. The NEB procedure was chosen since it has proven in our experience to be computationally robust in conjunction with a carefully chosen initial reaction path. NEB calculations were verified in a self-consistent manner, by restarting calculation while increasing the corresponding accuracy of convergence.

### 2.2. Methodology for determining rate of reactions and entropy

Rate of reactions for an overall reaction scheme was calculated by describing each individual reaction step using its corresponding kinetic barrier ($\Delta G$). The rate constant, $k$, for each forward and backward reaction was calculated based on the Eyring equation,

$$k = \frac{k_B T}{h} \exp\left(-\frac{\Delta G}{RT}\right) \tag{1}$$

and the Gibbs' free energy, $\Delta G$, of the corresponding kinetic barrier,

$$\Delta G = \Delta H - T\Delta S. \tag{2}$$

Here $k_B$ is Boltzmann constant, $h$ is Planck's constant, $R$ is the universal gas constant, $T$ is temperature, $\Delta H$ is enthalpy and $\Delta S$ is entropy. When calculating rate constants for barrierless reactions a zero energy barrier was assumed, thus basing the rate constant on the approximate pre-exponential factor of Eq. (1).

It is noted that entropy is composed of translational, rotational and vibrational components in which the first two contribute the greatest amount towards the overall entropy of a molecule in the gas phase. In the kinetic simulations presented in this work, it was assumed that the chemisorption of a gas phase species causes the complete loss of its translational and rotational entropies. The rationale behind this assumption is that a gas phase molecule adsorbed on a surface becomes immobile, thus substantially eliminating the entropies arising from its translational and rotational motions [36]. In addition, the accurate evaluation of the these entropies of an adsorbed species is not possible with VASP. On the other hand, the vibrational component of the overall entropy of surface species was neglected because it constitutes only a small portion of $\Delta S$ compared to the loss of the translational and rotational counterparts (e.g., $\Delta S_{vib}$ for CO is 0.003 kcal/mol while $\Delta S_{trans}$ and $\Delta S_{rot}$ are 14.9 and 4.8 kcal/mol, respectively, at 400 K). Thus, when calculating the Gibbs' free energy ($\Delta G$ of Eq. (2)) of a reaction on the surface, $\Delta S$ was assumed to be zero. On the other hand, for adsorption (desorption) reaction $\Delta S$ was calculated as the loss (gain) of translational and rotational entropy.

The calculated entropy (translational and rotational energy) data employed in the present simulations are $\Delta S_{trans+rot}$ $(O_2(g)) = 0.046885$ kcal/(mol K) and $\Delta S_{trans+rot}$ $(SO_2(g)) = 0.058375$ kcal/(mol K).

The individual rate constants derived from Eq. (1) were used to determine the time-dependent rate of formation of each species in the reaction scheme. Concentration of each individual species was calculated by integrating the respective rate of formation over time $t$ utilizing the mathematical software MatLab [37] which affords the simultaneous integration of multiple rate equations.

### 2.3. Methodology for continually stirred tank reactor (CSTR) kinetic model

All reactions occurring at the anode pertaining to the removal of previously adsorbed surface sulfur can be simulated using a CSTR kinetic model. This model describes each reaction step and its corresponding kinetic barrier as a differential equation regarding the rate of formation of individual species (Section 2.2). The set of differential equations are integrated numerically over time to obtain the concentrations of the various species as a function of time.

Our CSTR model could be considered as a chamber (mimicking the anode) with a volume of $1.35 \times 10^{-6}$ m$^3$, maintained at a temperature of 800 °C (typical SOFC operating temperature). The reactive surface within the CSTR had a $6.75 \times 10^{-1}$ m$^2$ surface area and a vacant adsorption site concentration of $7.72 \times 10^{-6}$ mol/m$^2$ (based on the number of 3f sites on a nickel(111) surface). Gaseous oxygen at pressure 1 atm continually flowed into the CSTR, and gaseous sulfur dioxide continually flowed out with a flow rate of 40 ml/min STP.

Inside the CSTR, gaseous species could adsorb and desorb from the surface, and adsorbed species could react with each other. The CSTR reactive surface was hypothetically dissected into small equally sized sections, each of which correspond to four nickel atoms and their surrounding space. Four nickel atoms per section were chosen to mimic the size of the nickel $(2 \times 2)$ unit cell used in our calculations. Each of these sections represented one vacant site on the CSTR surface. By means of this method we could consider steric interactions between adsorbed species on the CSTR surface. Adsorbing and dissociating species within one vacant site maintained the correct surface coverage within that adsorption site. For example, a 100% CSTR surface coverage of a 2*S species produces an overall surface with 50% sulfur coverage ($\theta_S = 0.50$ ML). Using this CSTR model the ever changing concentrations of all gaseous and adsorbed species pertaining to adsorption/desorption and dissociation/association reactions on the SOFC anode could be calculated until surface coverage equilibrium was reached.

## 3. Results and discussions

### 3.1. Configurations of sulfur-covered Ni(111)

The main objective of this work was to explore the regeneration of the Ni anode activity of SOFC by means of the oxidation by $O_2$ gas. In particular, this study focused on the treatment of the SOFC with $O_2$ after its operation has been shut off; in this situation, no $O^{2-}$ is continuously supplied via the solid electrolyte, and the $O_2$ gas injected into the chamber is the only source of oxygen. The surface coverage by sulfur pollutant was restricted to below 0.50 ML. Specifically, the coverage of 0.25 and 0.50 ML by sulfur were considered. It has been experimentally observed that the surface chemistry of $SO_2$ on Ni(111) is substantially different at these sulfur concentrations [38–40], although, to our knowledge, no experimental work has been devoted to the direct $O_2$ chemisorption on the S-precovered Ni(111) surface. Accordingly, we considered two separate sets of $O_2$ adsorption/$SO_2$ desorption reaction, one for each coverage,

$$2^*S + O_2(g) \leftrightarrow {}^*S + SO_2(g), \quad (3)$$

$${}^*S + O_2(g) \leftrightarrow [M] + SO_2(g). \quad (4)$$

Note that for the 0.25 ML coverage, the surface sulfur atoms were arranged in a $p(2 \times 2)$-S configuration which has been proven by both LEED experiments [22,41] and theoretical calculations [23]. At a higher coverage, however, more than one morphology have been reported: $p(2 \times 2)$, $(\sqrt{3} \times \sqrt{3})R30$, $(5\sqrt{3} \times 2)$ and $(8\sqrt{3} \times 2)$ [42]; among which the $(5\sqrt{3} \times 2)$ has been found to be stable at temperature around 1100 K accompanied by a large extent of surface reconstruction [43].

Despite the thermal stability of the $(5\sqrt{3} \times 2)$ configuration, we considered the more primitive $p(2 \times 2)$ surface structure to represent the sulfur-poisoned Ni(111) surface at the recoverable stage. It has been noticed that in all experimental studies regarding the sulfur-modified Ni(111) surface, the reaction of clean Ni(111) with $H_2S$ was performed in a high vacuum environment containing no oxygen. These conditions, however, are different from the Ni surface inside the anode chamber of SOFC where oxygen is continually provided through the electrolyte. It is believed that oxygen in the triple-phase boundary participate in removing the adsorbed S in form of $SO_2$, thus retarding the formation of a highly reconstructed $(5\sqrt{3} \times 2)$ phase.

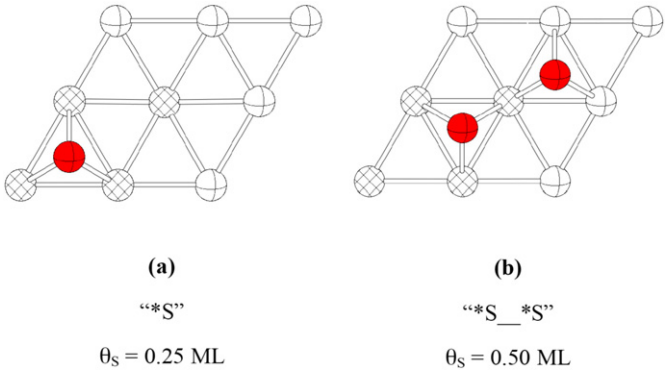


**Fig. 1.** Simplified geometries illustrating different amounts of adsorbed sulfur ($\theta_S$) on nickel planar surface. The orthorhombic unit cell is highlighted by patterned nickel atoms.

On the other hand, the thermal stability of the $(5\sqrt{3} \times 2)$ configuration at high temperature implies that this process is possibly irreversible. Moreover, the substantial reconstruction of the Ni surface from pure (111) to pseudo-(100) overlayer on (111) [44] may lead to the permanent change of cell activity. While these conditions correspond most likely to the irreversible phase of the cell deactivation, we are more interested in the initial reversible phase of sulfur poisoning of the Ni anode of SOFC [14]. Therefore, it is believed that the primitive $(2 \times 2)$ configuration should be a more appropriate model to represent the 0.50 ML sulfur coverage on Ni(111). The graphical representations of the 0.25 and 0.50 ML surfaces are given in Fig. 1.

Throughout the investigation of $O_2$ adsorption on S-precovered Ni(111), we excluded the possibility of multiple molecular oxygen adsorption or the migration of oxygen adatoms into the bulk, although these phenomena have been detected at >500 K for clean Ni surfaces [45]. Moreover, we considered only the adsorption of S at the most thermodynamically favorable three-fold sites on Ni(111) [23], since the diffusion of S atoms to lower-coordination sites results in a weakening of the surface Ni–S bonds which possibly renders a more favorable sulfur oxidation in the post-treatment.

We also neglected the oxygen diffusion on the Ni(111) surface during the oxidation because of the fact that oxygen binds very strongly to Ni (>60 kcal/mol); it is thus anticipated that the diffusion rate of surface oxygen atoms is very low. Furthermore, it is found that the dissociative adsorption of $O_2$ molecule on the sulfur-precovered Ni(111) surface readily generates available O adatoms adjacent to S (Figs. 1, 2, 4, 6), and thus the contributions of O diffusion to the rates of reactions between S and O are minimal.

We note again that our main interest is to describe the removal of the last 25% sulfur from a nickel surface by $O_2$, as observed experimentally [14]. At this coverage, no surface reconstruction has been experimentally detected as those seen when the coverage exceeds 0.50 ML at high temperatures. Consequently, we excluded the surface reorganization in the presence of sulfur adatoms.

### 3.2. Adsorption of $O_2$ followed by desorption of $SO_2$ on Ni(111) surface with initial sulfur coverage $\theta_S = 0.25$ ML

For an initial atomic sulfur surface with coverage of $\theta_S = 0.25$ ML, the adsorption of $O_2$ and subsequent desorption of $SO_2$ result in a change in sulfur surface coverage of 25% and a "clean" surface with no remaining adsorbed sulfur. Geometries for all

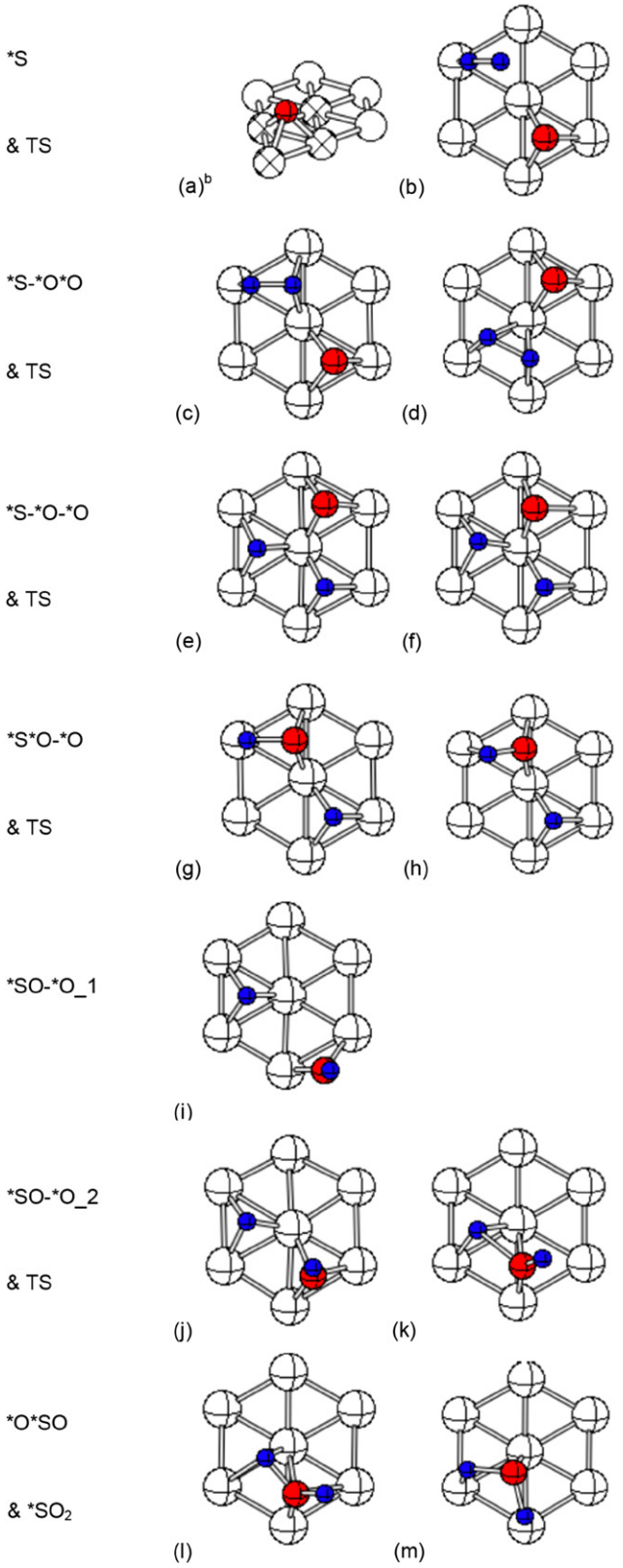


**Fig. 2.** Geometries corresponding to adsorption and dissociation of $O_2$ followed by association and desorption of $SO_2$ on S–Ni(111) surface with initial coverage $^{a}\theta_S = 0.25$ ML. ($^{a}$Adsorbed sulfur surface coverage; $^{b}(2 \times 2)$ supercell highlighted by patterned nickel nuclei.)

species corresponding to the surface coverage $\theta_S = \theta_{S,2O} = 0.25$ ML (S and S + 2O) are illustrated in Fig. 2 and the corresponding thermodynamic energies and kinetic barriers are stated in Fig. 3.

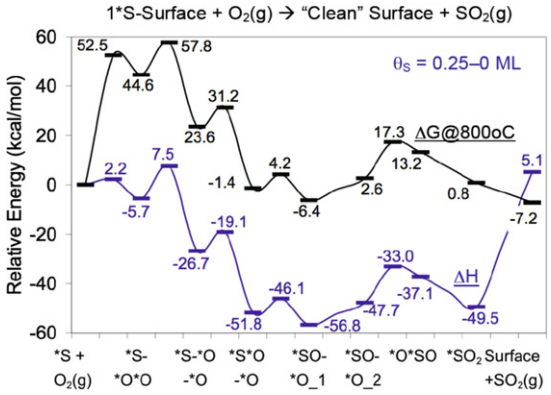


**Fig. 3.** Gibbs' free energy ($\Delta G$ at 800 °C, black line) and enthalpy ($\Delta H$, blue line) profile illustrating relative thermodynamic energy and kinetic pathway of $O_2$ adsorption and $SO_2$ desorption on S–Ni(111) surface with initial coverage $\theta_S = 0.25$ ML. (For interpretation of the references to color in this figure legend, the reader is referred to the web version of this article.)

The geometry corresponding to a pure 25% sulfur surface (*S, Fig. 2a) has been described in our earlier research [23]. Therefore, it is necessary only to repeat that sulfur preferentially adsorbs at a fcc 3-fold-hollow (3fh) site with Ni–S bond distances (×3) of 2.15 Å. The adsorption of $O_2$ on a nickel surface with an initial atomic sulfur coverage of 25% is dissociative in nature. After overcoming an adsorption transition state (TS, Fig. 2b), a precursor state is created where the oxygen's are bound to the surface within one hcp 3-fold-filled (3ff) adsorption site, as well as to each other (*S–*O*O, Fig. 2c). This illustrates oxygen adsorbed at adjacent one-fold/on-top (1f) and two-fold/bridge (2f) sites within the 3ff geometry. Elongation of the oxygen–oxygen bond is observed upon adsorption, resulting in an $O_{1f}$–$O_{2f}$ bond distance of 1.39 Å (compared to the gas phase distance of 1.23 Å). Corresponding Ni–O1f and Ni–O2f bond distances are 1.88 Å and (×2) 1.96 Å, respectively, while Ni–S bond distances are 2.08 Å and (×2) 2.14 Å.

A second TS (Fig. 2d) results in the dissociation of the O–O bond followed by migration of the individually adsorbed oxygen to adjacent 3fh positions (*S–*O–*O, Fig. 2e). The same dissociative adsorption mechanism is found in the literature for $O_2$ adsorption on a "clean" ($\theta_S = 0$ ML) nickel surface [46]. Corresponding adsorbed sulfur and oxygen's within the *S–*O–*O species are in the most optimum geometry to reduce steric hindrance. Despite this, the close positioning of *S and 2*O on the surface leads to weakening of the Ni–S bonds, demonstrated by Ni–S bond elongation. Ni–$O_{3fh}$ bond distances are 1.81–1.87 Å and Ni–$S_{3fh}$ bond distances are 2.12–2.18 Å.

Migration of *O and *S groups, from adjacent 3fh sites to a central 3ff position, leads to the formation of a S–O bond parallel (∥) to the surface (TS, *S*O–*O; Fig. 2, f and g, respectively). Fig. 2f with the S–$O_{\parallel}$ bond, where the *S and *O are adsorbed at corresponding 2f and 1f sites within the central 3ff position, exhibits the following $S_{2f}$–$O_{1f/\parallel}$, Ni–$O_{1f}$, Ni–$S_{2f}$ and Ni–$O_{3fh}$ bond distances: 1.55 Å, 2.01 Å, (×2) 2.14 Å and 1.81–1.85 Å, respectively. S–O bond rotation within the species *S*O–*O results in the formation of *SO–*O1, where the previously parallel S–O bond is now positioned perpendicular (⊥) to the surface (TS, *SO–*O1; Fig. 2, h and i, respectively). Now the Ni–$SO_{3ff/\perp}$ and S–$O_{\perp}$ bond distances are 2.06–2.09 Å and 1.47 Å, respectively, while Ni–$O_{3fh}$ bond distances remain the same at 1.81–1.84 Å. The closest distance between *$SO_{3ff/\perp}$ and *$O_{3fh}$ within species *SO–*O1 is 3.05 Å.

Migration of *$SO_{\perp}$, from a 3ff to an adjacent 3fh position, produces a second *SO–*O-type geometry where all atoms adsorbed directly to the surface are in 3fh sites (*SO–*O2, Fig. 2j). No transition state was determined between species *SO–*O1 and *SO–*O2. Within species *SO–*O2, a distance of only 2.83 separates *$SO_{3fh/\perp}$

and $^*O_{3fh}$. Bond distances describing Ni–$SO_{3fh/\perp}$ and Ni–$O_{3fh}$ have generally elongated (2.05–2.20 Å and 1.78–1.90 Å, respectively) to accommodate the greater steric hindrance brought on by the closer proximity of the species. The corresponding S–$O_\perp$ bond distance remains the same at 1.47 Å.

Migration of $^*SO_{3fh/\perp}$ and $^*O_{3fh}$ towards a central 3ff site gives rise to the formation of a second S–O bond, parallel to the surface (TS, *O*SO; Fig. 2, k and l, respectively). The resulting geometry resembles a perpendicularly adsorbed $^*SO_2$ species. Sulfur is adsorbed at a 2f position, with one oxygen adsorbed at an off-1f site parallel to the surface and the remaining oxygen adsorbed nearly perpendicular to the surface. Ni–$S_{2f}$ (×2), $S_{2f}$–$O_{1f/\parallel}$, $S_{2f}$–$O_\perp$ and Ni–$O_{1f}$ bond distances are 2.11, 2.40, 1.54, 1.45 and 2.09 Å, respectively. This distorted $^*SO_2$ species rotates to lie with its O–S–O plane parallel to the surface in an adjacent 3ff adsorption site, where both the S and the O atoms are situated in near 1f positions ($^*SO_2$, Fig. 2m). Corresponding bond distances for Ni–S, Ni–O1 (previously $SO_\parallel$) and Ni–O2 (previously $SO_\perp$) are 2.18, 2.03 and 1.54 Å, respectively. S–O bond distances within the $^*SO_{2/\parallel}$ species are (×2) 1.54 Å, demonstrating considerable bond elongation compared to the respective bond distances in the gas phase (1.42 Å). Comparing the bond strength of S–O between the gas phase and molecularly adsorbed species; an experimentally and theoretically observed elongation of the bond is ascribed to the charge transfer from the occupied Ni 3d bands to the antibonding $SO_2$ $\pi^*$ orbitals, leading to a weakening of the S–O bond [47]. No transition state was determined between species *O*SO and $^*SO_2$. The planar 3f $^*SO_2$ species described above is almost identical to that determined experimentally in the literature and briefly described in the introduction [40,48,49]. Within this pathway and corresponding surface coverage the remaining reaction follows the desorption of the $SO_2$ species from the surface. By their very nature, a pre-requisite to the formation of any minima species is a TS. Our inability to locate certain TS structures within this reaction pathway is not an indication that our minima structures are incorrect, simply that the TS energy barrier is very small.

Fig. 3 illustrates the enthalpy ($\Delta H$, blue line) and Gibbs' free energy ($\Delta G$ at 800 °C, black line) reaction profile corresponding to the $O_2/SO_2$ adsorption and desorption reaction on a nickel surface with an initial sulfur coverage of $\theta_S = 0.25$ ML. Without the inclusion of entropy, at 0 K (−273 °C), the enthalpy pathway describes an overall endothermic process (5.1 kcal/mol). Adsorption of $O_2$, producing the precursor state *S–*O*O, is thermodynamically less stable in the presence of adsorbed surface sulfur. The exothermic reaction $n^*S$–surface + $O_2 \leftrightarrow n^*S$–$^*O_2$ releases 32 kcal/mol when $n = 0$ ($\theta_S = 0$ ML) [46] and 6 kcal/mol when $n = 1$ ($\theta_S = 0.25$ ML, Fig. 3). This indicates that the presence of sulfur weakens oxygen adsorption on the surface. Several intermediates preclude the formation of the most stable species found on this pathway, *SO–*O1 describing perpendicularly orientated $^*SO_{3ff/\perp}$ and $^*O_{3fh}$, with the energy of −56.8 kcal/mol relative to 25% sulfur surface coverage and $O_2$(g). Overcoming an energy barrier of ∼25 kcal/mol produces a slightly less thermodynamically stable species, $^*SO_2$, with a corresponding relative energy of −49.5 kcal/mol. At a temperature of 0 K endothermic molecular desorption (54.6 kcal/mol) produces $SO_2$(g) and a "clean" surface ($\theta_S = 0$ ML). This concurs with experimental literature that observes stable $SO_2$ molecular adsorption at temperatures <200 K [47,50].

Carrying out this reaction at the high temperatures usually associated with SOFCs alters the energy pathway considerably. The Gibbs' free energy profile at 800 °C demonstrates an overall exergonic process (−7.2 kcal/mol), with the most stable intermediate/product species being the desorption of $SO_2$ and the production of a "clean" surface ($\theta_S = 0$ ML). When comparing Gibbs' free energies, the most stable species on the enthalpy profile (*SO–*O1) is less stable than the product (surface + $SO_2$(g)) by 0.8 kcal/mol.

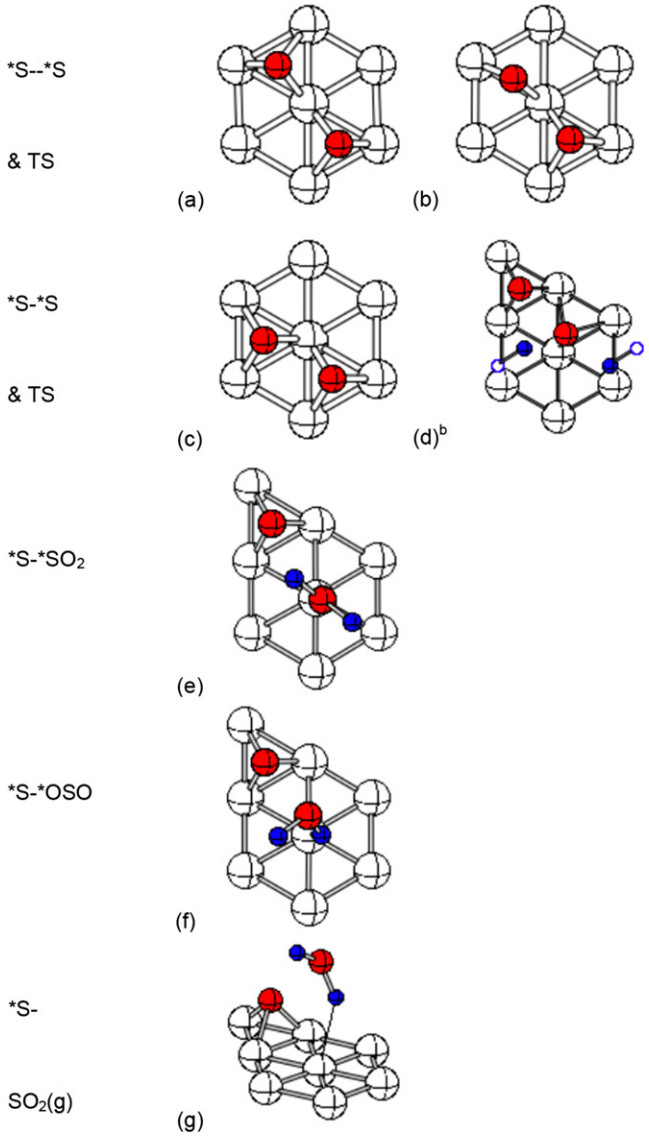


**Fig. 4.** Geometries corresponding to adsorption and dissociation of $O_2$ followed by association and desorption of $SO_2$ on S–Ni(111) surface with initial coverage [a]$\theta_S = 0.50$ ML. ([a]Adsorbed sulfur surface coverage; [b]colored hollow atoms represent repeated atoms in adjacent supercell.)

The driving force behind the burning and removal of elemental surface sulfur as $SO_2$ is the exergonic reaction producing the most stable species after $SO_2$ desorption.

### 3.3. Adsorption of $O_2$ followed by desorption of $SO_2$ on Ni(111) surface with initial sulfur coverage $\theta_S = 0.50$ ML

The adsorption of $O_2$ and subsequent desorption of $SO_2$, on an initial atomic sulfur coverage of $\theta_S = 0.50$ ML, describes a reduction in sulfur by 25%, producing a remaining coverage of $\theta_S = 0.25$ ML. Geometries for all species corresponding to a surface coverage of $\theta_S = \theta_{S,O} = 0.50$ ML (2S and 2S + 2O) are illustrated in Fig. 4 and corresponding thermodynamic energies and kinetic barriers are stated in Fig. 5. We note that a nickel surface of $\theta_S = 0.50$ ML sulfur coverage appears to form under SOFC conditions when the fuel contains small amount (5 ppm) of $H_2S$ [51].

Adsorption of $O_2$ on the $\theta_S = 0.50$ ML surface involves a substantial amount of steric hindrance. Adsorption occurs on the *S–*S species, maintaining adequate available space in preparation for the introduction of $O_2$ while producing the least amount of

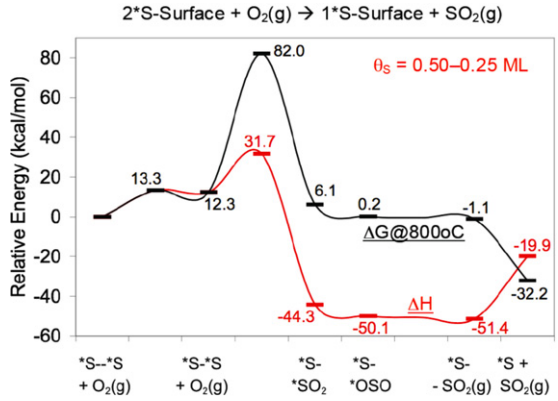


**Fig. 5.** Gibbs' free energy ($\Delta G$ at 800 °C, black line) and enthalpy ($\Delta H$, red line) profile illustrating relative thermodynamic energy and kinetic pathway of $O_2$ adsorption and $SO_2$ desorption on S–Ni(111) surface with initial coverage $\theta_S = 0.50$ ML. (For interpretation of the references to color in this figure legend, the reader is referred to the web version of this article.)

steric hindrance between the adsorbed species. Unlike the previous $\theta_S = 0.25$ ML surface, adsorption occurs dissociatively at adjacent 3fh–3ff positions without the presence of a precursor state. Due to the close proximity of the surface sulfur atoms, formation of the $SO_2$ occurs in a one-step process (TS, $^*S$–$^*SO_2$, Fig. 4, d and e, respectively). Fig. 4e is the geometry of the initial perpendicular $^*SO_2$ species adsorbed at a 1f site. The corresponding Ni–$S_{1f}$ bond distance is 2.28 Å, with $S_{1f}$–$O_\perp$ bond distances of (×2) 1.45 Å and an O–S–O bond angle of 115.9°. The individually adsorbed sulfur atom has Ni–$S_{3fh}$ bond distances between 2.11–2.14 Å. An elongated S–S minimum distance of 3.10 Å, after the formation of the $SO_2$ group, illustrates that sterics is the main driving force behind this one-step process.

Upon the production of the $^*S$–$^*SO_2$ species, the atoms on the surface orientate themselves in a way that reduces steric hindrance, by leaving as much space as possible between the adsorbed atoms. While maintaining the current $SO_2$ geometry, a further step in the reaction pathway rotates the $SO_2$ group so that it is adsorbed to the surface at the previously observed 1f coordination site via an oxygen atom ($^*S$–$^*OSO$, Fig. 4f). Corresponding Ni–$O_{1f}$, $O_{1f}$–S and S–O bond distances are 2.13, 1.48 and 1.46 Å, respectively, with an O–S–O bond angle of 115.2°. While the geometry of the $SO_2$ group remains approximately the same, an increase in the Ni–S bond distances of the remaining individually adsorbed S atom occurs (N–$S_{3fh}$ are 2.14–2.17 Å). A minimum S–S distance of 2.95 Å demonstrates a slight decrease in distance when compared to the previous structure.

The penultimate reaction step desorbs $SO_2$ from the 1f adsorption site, but maintains the molecule physisorbed to the surface ($^*S$–$SO_2$(g), Fig. 4g). The resulting Ni···OSO ($SO_2$(g)) distance is 3.11 Å, with S–O bond distances of (×2) 1.45 Å and an O–S–O bond angle of 118.0°. Remaining Ni–$S_{3fh}$ bond distances are all equal at (×3) 2.15 Å, producing a minimum S–S distance of 4.33 Å. No transition states were located between species $^*S$–$^*SO_2$, $^*S$–$^*OSO$ and $^*S$–$SO_2$(g). As previously described (Section 3.2) this indicates the presence of very small energy barriers between the calculated minima.

The geometries of all species with a coverage of $\theta_{S,O} = 0.50$ ML (2S + 2O) are very different from those at the coverage of $\theta_{S,O} = 0.25$ ML (1S + 2O). Based on the similar conclusions determined during comparison of different $SO_2$ surface coverage in experimental literature, geometrical differences could be due to the attractive intermolecular interactions only observed at high coverage, as well as the steric interactions caused by dense packing [52].

Fig. 5 illustrates the enthalpy ($\Delta H$, red line) and Gibbs' free energy ($\Delta G$ at 800 °C, black line) reaction profile corresponding to the $O_2/SO_2$ adsorption/desorption reaction on a nickel surface with an initial sulfur coverage of $\theta_S = 0.50$ ML. An overall strongly exothermic process (−19.9 kcal/mol) is demonstrated by the $\Delta H$ pathway with no entropic contributions. The most stable reaction species corresponds to the physisorption of $SO_2$(g) to the surface, $^*S$–$SO_2$(g), at −51.4 kcal/mol. The rate-determining reaction step at this surface coverage at 0 K is the complete endothermic desorption of the $SO_2$(g) molecule, requiring an energy of 31.5 kcal/mol and resulting in the production of a 25% sulfur surface coverage ($^*S$, Fig. 2a).

At higher temperatures (800 °C), the inclusion of entropy alters the reaction profile by substantially increasing the energy barrier associated with $O_2$ adsorption that causes $SO_2$ desorption to become considerably exergonic. Overall, the formation of $SO_2$(g) and a 0.25 ML of elemental surface sulfur ($\theta_S = 0.50$–0.25 ML) releases 32.3 kcal/mol of energy. This is a much stronger exergonic reaction than the corresponding result on a lower sulfur surface coverage, $\theta_S = 0.25$–0 ML (−7.2 kcal/mol). Due to surface steric hindrance, adsorption of $O_2$ occurs via a considerably larger TS energy barrier (69.8 kcal/mol) compared to an initial surface coverage of $\theta_S = 0.25$ ML (52.5 kcal/mol). Upon adsorption, the species $^*S$–$^*SO_2$ is instantly formed and in-turn re-orientates the $SO_2$ group to produce $^*S$–$^*OSO$. Elongation of the Ni–OSO bond initially creates an $SO_2$(g) physisorbed species until, finally, desorption occurs in an exergonic manner. A final reaction step, desorbing $SO_2$ and producing a surface coverage of $\theta = 0.25$ ML, releases 31.1 kcal/mol of energy. This is considerably larger then the corresponding reaction step producing a "clean" surface, $\theta_S = 0$ ML, which releases energy of only 8.0 kcal/mol.

Based on the Gibbs' free energy data, our investigation demonstrates that at high temperatures (800 °C) $SO_2$ desorption is more favorable at larger surface coverage of sulfur up to 0.50 ML. Overall, after the adsorption of $O_2$ on an initial $\theta = 0.50$ ML surface of elemental sulfur, a considerable part of the driving force behind the desorption of $SO_2$ is the large steric hindrance caused by the close proximity of the adsorbed atoms. The steric interaction facilitates the formation of the $^*SO_2$ group via a substantially exergonic reaction.

It should be noted that on an initial $\theta_S = 0.50$ ML atomic sulfur surface, other adsorption geometries for $O_2$ were studied but were noticed to have TS barriers that were too high, even without the inclusion of entropy. Formation of precursor states and other adsorption minima, for example $^*O^*O$ adsorption within a 3f site ($^*O_{1f}$–$^*O_{2f}$ as previously demonstrated for the $\theta_{S,2O} = 0.25$ ML surface) and $^*O^*O$ adsorption in adjacent 3fh–3ff positions, were found to have relative minima energies of ∼90 kcal/mol and all were precluded by adsorption TS with the corresponding relative energies of ∼120 kcal/mol. The only other feasible reaction pathway (Figs. 6 and 7) calculated involved the immediate formation of the species $^*SO_{3fh/\parallel}$–$^*SO_{3fh/\perp}$ (relative $\Delta G_{TS} = 88.6$ kcal/mol, $\Delta G = 36.8$ kcal/mol, Fig. 6, a and b, respectively) after the adsorption of $O_2$. In turn, this produced the species $^*S_{3fh}{}^*SO_{1f/\perp}$–$^*O_{3fh}$ (relative $\Delta G_{TS} = 53.7$ kcal/mol, $\Delta G = 24.5$ kcal/mol, Fig. 6, c and d, respectively), followed by the previously described minima $^*S$–$^*OSO$ (relative $\Delta G_{TS} = 25.4$ kcal/mol, Fig. 6e and $\Delta G = 0.2$ kcal/mol, Fig. 6f). While this pathway is energetically very similar in nature to the pathway described above and illustrated in Fig. 5, the energy required to overcome the TS energy barriers is much larger. It therefore makes this pathway not as likely as the others described above.

### 3.4. Desorption of $S_2$ on Ni(111) surface with initial sulfur coverage $\theta_S = 0.50$ ML

Our research investigated the formation and desorption of elemental sulfur ($S_2$(g)), with entropic contributions, as a means

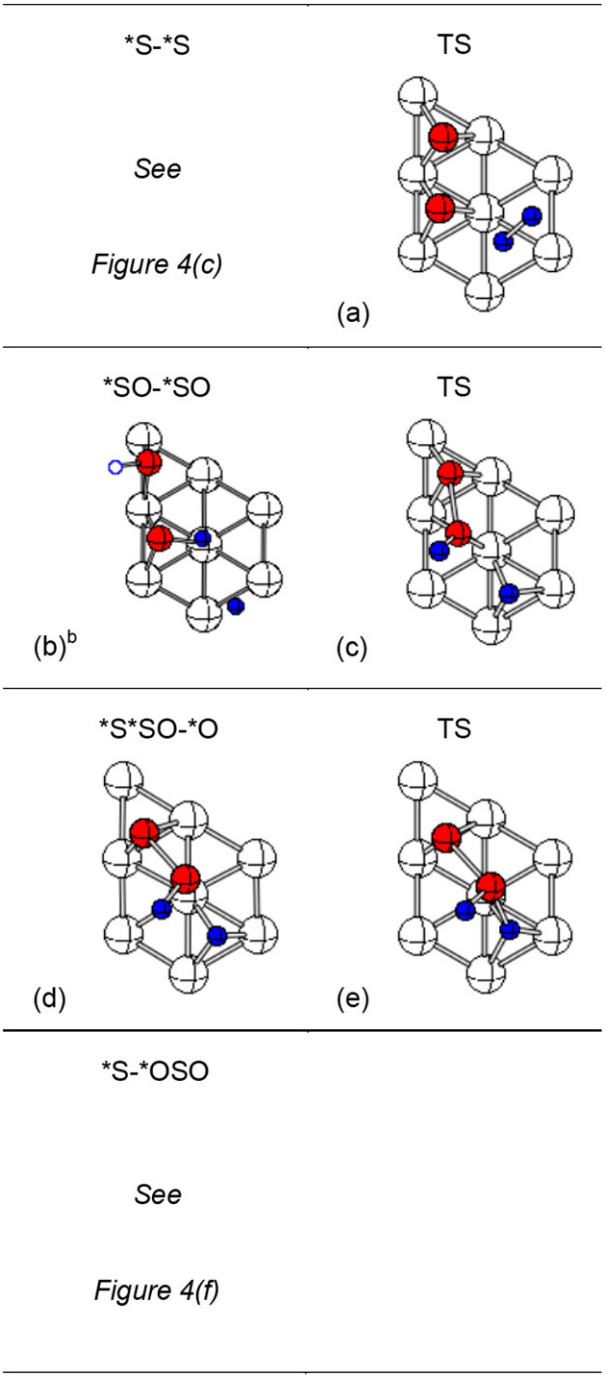


**Fig. 6.** Geometries corresponding to alternative pathway for adsorption and dissociation of $O_2$ followed by association and desorption of $SO_2$ on S–Ni(111) surface with initial coverage [a]$\theta_S = 0.50$ ML. ([a]Adsorbed sulfur surface coverage; [b]colored hollow atoms represent repeated atoms in adjacent supercell.)

of removing the strongly adsorbed sulfur from the nickel surface. Based on the size of the supercell used within these calculations ($2 \times 2$), the desorption of $S_2$ from the surface must be considered at an atomic sulfur coverage of at least $\theta_S = 0.50$ ML (i.e. 2 S:4 Ni). At a coverage of 0.50 ML, $S_2$ desorption is demonstrated to be strongly endergonic (40.3 kcal/mol) with inconsequential kinetic barriers (Fig. 7). In previous sections of this paper, the presence of several adsorbed sulfur atoms in close proximity to each other has been established to be the cause of substantial steric effects between the adsorbed atoms. Due to this, desorption of $S_2$ is highly improbable as large amounts of energy must be introduced into

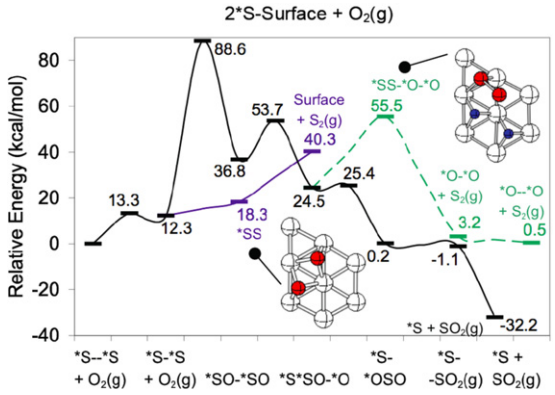


**Fig. 7.** Alternative relative thermodynamic energies and kinetic pathways (Gibbs' free energy, $\Delta G$) of Ni(111) surface with initial atomic sulfur coverage of $\theta_S = 0.25$ ML. The three profiles represent $S_2$ desorption without the presence of oxygen ($\theta_S = 0.50$–0 ML, purple line), $O_2$ adsorption followed by $S_2$ desorption ($\theta_S = 0.50$–0 ML, green line) and $O_2$ adsorption followed by the alternative reaction pathway to $SO_2$ desorption ($\theta_S = 0.50$–0.25 ML, black line). A dashed line represents thermodynamic data only. (For interpretation of the references to color in this figure legend, the reader is referred to the web version of this article.)

the system before the reaction can occur. Further research studied the possibility of desorbing $S_2$ in the presence of oxygen at a coverage of $\theta_{S,O} = 0.50$ ML (i.e. 2 O:2 S:4 Ni). Overall, adsorption of $O_2$ followed by the desorption of $S_2$ is a slightly endergonic reaction with the reaction energy of 0.5 kcal/mol (Fig. 7). The removal of $S_2$ in the presence of oxygen initially follows the alternative pathway previously described for the removal of $SO_2$(g) at a sulfur surface coverage of 0.50 ML (Figs. 5 and 7). Comparing $SO_2$ and $S_2$ desorption, based purely on thermodynamic energy profiles, the removal of $S_2$(g) in the presence of oxygen requires an extra energy input >30 kcal/mol after the formation of species *S*SO–*O (Fig. 6d). Due to the immediate formation and the strongly exergonic nature of the *$SO_2$ group (Figs. 5 and 7), it is highly unlikely that $S_2$ would be given the opportunity to associate and desorb in this endergonic manner.

### 3.5. Consecutive adsorption/desorption of $O_2/SO_2$ on a S–Ni(111) surface with initial sulfur coverage of $\theta_S = 0.50$ ML

Based on previously described calculations within this account (Sections 3.2 and 3.3), an overall reaction scheme (Eqs. (5)–(9)) can be considered for the removal of atomic surface sulfur with an initial coverage of $\theta_S = 0.50$ ML via desorption of $SO_2$. This reaction mechanism considers the adsorption and dissociation of $O_2$, followed by the association and desorption of $SO_2$ to produce a surface coverage of 25% sulfur (Eqs. (5) and (6)). Further adsorption and complete dissociation of $O_2$, at this coverage of $\theta_S = 0.25$ ML, is described by Eq. (7). While Eq. (8) is concerned with the association of the species *SO–*O, Eq. (9) considers the formation and desorption of $SO_2$ to produce a "clean" surface ($\theta_S = 0$ ML).

$$*S{-}{-}*S \leftrightarrow *S{-}*S, \tag{5}$$

$$*S{-}*S + O_2 \leftrightarrow *S{-}*OSO \leftrightarrow *S{-}SO_2 \leftrightarrow *S + SO_2, \tag{6}$$

$$*S + O_2 \leftrightarrow *S{-}*O*O \leftrightarrow *S{-}*O{-}*O, \tag{7}$$

$$*S{-}*O{-}*O \leftrightarrow *S*O{-}*O \leftrightarrow *SO{-}*O1 \leftrightarrow *SO{-}*O2, \tag{8}$$

$$*SO{-}*O2 \leftrightarrow *O*SO \leftrightarrow *SO_2 \leftrightarrow \text{surface} + SO_2. \tag{9}$$

The relative energy profile for this reaction scheme (Eqs. (5)–(9)), concerning enthalpy ($\Delta H$, colored line on graph) and Gibbs' free energy ($\Delta G$ at 800 °C, black line on graph), is illustrated in Fig. 8. Individual enthalpy and Gibbs' free energy profiles for the different initial atomic sulfur surface coverage (0.25 ML and 0.50 ML) have

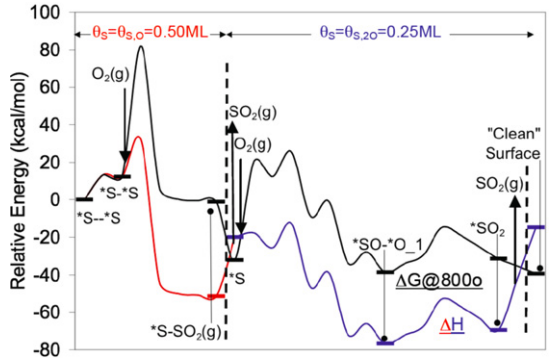


**Fig. 8.** Relative energy pathway following consecutive adsorption/desorption of $O_2/SO_2$ from an initial coverage of $\theta_S = 0.50$ ML (Eqs. (5)–(9)). Energy profile illustrated without entropy contributions (enthalpy, $\Delta H$, colored line) and including entropy contributions (Gibbs' free energy, $\Delta G$, black line). (For interpretation of the references to color in this figure legend, the reader is referred to the web version of this article.)

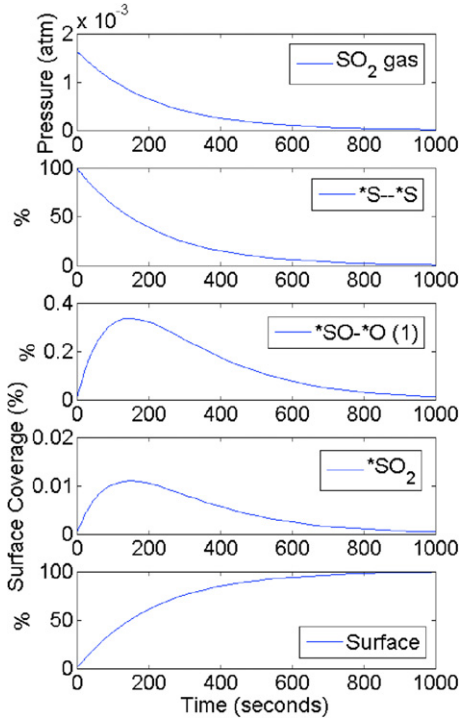


**Fig. 9.** Surface coverage of selected species determined by kinetic CSTR model at 800 °C, based on Eqs. (5)–(9).

been discussed in detail in previous sections. The Gibbs' free energy profile allows us to consider the reactions at a typical SOFC temperature of 800 °C. From the illustration in Fig. 8, it can be seen that despite a substantially large oxygen adsorption barrier, the driving force to remove the first 25% of adsorbed sulfur is the actual desorption of $SO_2$ which overall is a considerably exergonic reaction ($\theta_S = 0.50$–$0.25$ ML, $\Delta G = -32.2$ kcal/mol). The removal of the remaining 25% surface sulfur via $SO_2$ is exergonic by only a small amount ($\theta_S = 0.25$–$0$ ML, $\Delta G = -7.2$ kcal/mol). Comparing all the surface structures formed within the overall reaction profile $\theta_S = 0.50$–$0$ ML, the final desorption of $SO_2$ produces the most thermodynamically stable species ($\Delta G = -39.4$ kcal/mol). However, partial dissociation of $^*SO_2$ produces a structure with almost comparable exergonic stability ($^*$SO–$^*$O1, $\Delta G = -38.7$ kcal/mol). Based solely on the Gibbs' free energy data, the removal of the first 25% sulfur coverage ($\theta_S = 0.50$–$0.25$ ML) is only thermodynamically feasible if the initial oxygen adsorption barrier energy does not prove to be too large. However, from Fig. 8 alone, it is unclear as to whether the complete removal of the remaining 25% surface sulfur will occur ($\theta_S = 0.25$–$0$ ML) due to the comparable thermodynamic energies of the $^*$SO–$^*$O1 and the product species.

In order to establish whether removal of elemental surface sulfur will occur via the multiple adsorption/desorption of $O_2/SO_2$, respectively, on an initial surface coverage of $\theta_S = 0.50$ ML, a Continually Stirred Tank Reactor (CSTR) kinetic model was used. $O_2/SO_2$ adsorption/desorption on a SOFC anode was mimicked by introducing a constant supply of oxygen into the closed tank reactor model, allowing any corresponding adsorption, dissociation, association and desorption reactions to occur on an initial atomic sulfur surface, before removing a constant supply of sulfur dioxide product from the system. Based on the corresponding energy barriers for each reaction, including entropic contributions for the gas phase molecules, the rate of formation of individual species was used to calculate the continually altering concentrations of all reactant, intermediate and product species within the reaction profile at every time point until surface equilibrium is obtained.

The Gibbs' free energy profile for the above equations illustrates barrierless $SO_2$ desorption reactions (Eqs. (5)–(9), Fig. 8). Several methods exist to accurately calculate rate constants, and ultimately rate of formations, corresponding to barrierless adsorption/desorption reactions. These are usually associated with transition state theory or the Langmuirian adsorption model. While the CSTR kinetic model allows us to study the continually altering concentrations of all the reaction species, it is the final concentrations upon reaching equilibrium that are comparable to experimental observations. At equilibrium the rate of formation of the individual species does not alter; therefore, it is acceptable to calculate rate constants for barrierless $SO_2$ desorption reactions based solely on the approximate pre-exponential factor. Based on data calculated for Eqs. (5)–(9) ($\theta_S = 0.50$–$0$ ML, illustrated in Fig. 8), a reaction profile at 800 °C was modeled where the initial atomic sulfur surface coverage was set at $\theta_S = 0.50$ ML and the corresponding anode fuel comprised of 1 atm of $O_2$(g) (Fig. 9). Surface coverage was accomplished by specifying a 100% CSTR surface coverage of the species $^*$S–$^*$S, associated with a sulfur coverage of 50%.

We want to emphasize that the kinetic model does not consider the consecutive adsorption of oxygen molecules on the sulfur-precovered Ni(111) surface. Based on the thermodynamic profiles illustrated in Fig. 8, it is observed that the process of dissociative adsorption of $O_2$ in the presence of surface sulfur is highly endothermic; it is therefore expected that the second dissociative adsorption of $O_2$ is even less competitive to the recombination of surface S and O adatoms yielding $SO_2$ molecules. Accordingly, we postulated that the direct oxidation of the Ni(111) surface does not commence until the desulfurization process is approaching the completion.

Initially, at a time of ~10 s, a maximum amount of $SO_2$(g) is produced ($1.6 \times 10^{-3}$ atm) corresponding to the constant formation of the surface species $^*$S from an initial $\theta_S = 0.50$ ML surface ($2^*$S). As the time increases to ~120 s, maximum surface coverage of the individual species $^*$S, $^*$SO–$^*$O1 and $^*SO_2$ are obtained (0.002, 0.33 and 0.01%, respectively). Corresponding $^*$S–$^*$S species is substantially reduced to a coverage of 56%, while the amount of "clean" surface ($\theta_S = 0$ ML) coverage produced has increased (43%) at a constant rate. A non-existent concentration build-up of $^*$S, coupled with the continued production of $SO_2$(g) and the substantial decrease in the coverage of species $^*$S–$^*$S, demonstrates that the large barriers to oxygen adsorption are not detrimental to the overall reaction at either initial surface coverage of elemental sulfur (0.25 ML and 0.50 ML).

The time line produced during this model suggests that, initially, the reaction mechanism associated with the $O_2/SO_2$ adsorption/desorption reaction with differing sulfur coverage $\theta_S =$

0.50–0.25 ML is dominant. However, as the reaction proceeds the reduction in the rate of $SO_2$(g) produced and the maximum coverage obtained by species with a surface coverage of $\theta_{S,2O} = 0.25$ ML leads us to believe that the dominant mechanism at this later time is that associated with the corresponding $\theta = 0.25$–0 ML $O_2/SO_2$ adsorption/desorption reaction. The Gibbs' free energy difference between *SO–*O1 and the more stable product species ("clean" surface + $SO_2$(g)) is very small (0.8 kcal/mol), but is bridged by a TS energy barrier of ~25 kcal/mol. Due to the build-up in surface concentration of certain preceding species, especially *S–*S and *SO–*O1, this energy barrier is overcome to produce a "clean" surface with no remaining adsorbed sulfur atoms. Surface equilibrium is obtained upon complete removal of all sulfur-based surface species. This kinetic model indicates that at 800 °C on a SOFC nickel anode surface, it is completely feasible to envisage the burning and removal of all elemental surface sulfur via the formation of $SO_2$ under these conditions.

### 3.6. Comparing TPD and XPS experimental observations with theoretical calculations for nickel surfaces

Both TPD and XPS experiments observed no desorption of $SO_2$ below 600 K on the Ni(110) surface precovered by 0.25 ML $SO_2$; instead, a decomposition process leading to the formation of *SO and *O was detected [52]. A similar situation was also noticed by XPS on $SO_2$-covered Ni(111) at room temperature, in which $*SO_3$ is formed from the dissociation–recombination of $SO_2$ [39,40]. At higher coverage, however, desorption of $SO_2$ was observed at 300–400 K for Ni(110) [52], while no work has yet been undertaken for Ni(111).

Our present work, on the other hand, concludes that at temperatures of ~800 °C (1073 K), oxygen adsorption on an initial atomic sulfur 0.50 ML surface initiates the formation and desorption of $SO_2$, producing a remaining surface coverage of 25% sulfur. Further $O_2$ adsorption on the remaining 25% atomic sulfur surface initially produces the species *SO–*O, followed by removal of $SO_2$(g).

It initially appears that the present data contradict the published experimental investigations. Thus, although our results concerning the occurrence of $SO_2$ desorption at initial atomic sulfur coverage of 50% correlate to the experimental TPD data, no $SO_2$ desorption was observed experimentally up to a temperature of 600 K via TPD for an initial coverage of $\theta_{SO_2} < 0.25$ ML in contrast to our calculations. This discrepancy can be rectified after the recalculations of our Gibbs' free energy data for an initial $\theta_S = 0.25$ ML surface at temperatures between 600–1073 K. Based on the different reaction energy profile at the lower coverage, the formation of $SO_2$(g) on an initial $\theta_S = 0.25$ ML surface is exergonic only upon reaching a much higher temperature than that observed for the corresponding $\theta_S = 0.50$ ML surface. Therefore, our results concur with TPD data that observes no $SO_2$(g) formation at temperatures below 600 K.

XPS experimental data determines the complete dissociation of $SO_2$ at temperatures of ~370 K, based on an initial coverage of $\theta_{SO_2} = 0.25$ ML. It should be noted that at a temperature range of 270–370 K the surface dissociation reaction that is observed experimentally is $3*SO_2 \leftrightarrow 2*SO_3 + *S$. This dissociation reaction was not investigated during our theoretical studies as the species $*SO_3$ is not observed on a nickel surface at typical SOFC operating temperatures (800–1000 °C). After recalculating our Gibbs' free energy profile for the initial $\theta_S = 0.25$ ML surface at 370 K, the most thermodynamically stable species produced is of the type *SO–*O, which can be considered to illustrate partial dissociation of $SO_2$. This is consistent with observations by other experimental groups that illustrated the occurrence of molecular adsorption of $SO_2$ and a corresponding saturation coverage after $SO_2$(g) adsorption of ~0.50 ML at temperatures <200 K [47].

While the above comparison does demonstrate certain inconsistencies between theoretical and experimental data, the overall conclusions concerning the exergonic/endergonic nature of the overall reaction are still correct. The published experimental investigations give insight into $SO_2$ surface decomposition reactions at high temperatures, but they cannot accurately describe the surface reactions that will occur on the SOFC anode upon adsorption/desorption of $O_2/SO_2$ at consistently high temperatures.

## 4. Conclusions

Using periodic DFT calculations, we have demonstrated that the removal of adsorbed sulfur from a planar nickel (111) surface in the post-treatment of SOFC can be achieved via the systematic adsorption of molecular oxygen followed by the desorption of sulfur dioxide at initial atomic sulfur surface coverage's up to 50%. Adsorption and dissociation of $O_2$ on initial sulfur coverage of 50% at 800 °C leads to the immediate association of the $*SO_2$ species followed by the desorption of $SO_2$(g). This reaction produces an overall relative Gibbs' free energy of −32.2 kcal/mol relative to the energy of $O_2$(g) and a surface with 50% sulfur coverage. Under these conditions the most stable species in the reaction pathway corresponds to the production of $SO_2$(g) and an atomic sulfur surface coverage of 25%. Further adsorption and dissociation of $O_2$, on the resulting surface at the same temperature, produces the stable species *SO–*O1 with a relative Gibbs' free energy of −38.6 kcal/mol. Subsequent association and desorption of the remaining sulfur species, as $*SO_2$, occurs with an overall relative energy of −39.4 kcal/mol to produce the most energetically stable species of the overall Gibbs' free energy profile, consisting of a "clean" surface (no adsorbed sulfur-based species) and $SO_2$(g).

The reaction profile determined by the Gibbs' free energy for the multiple $O_2/SO_2$ adsorption/desorption reactions, respectively, on an initial atomic sulfur coverage of 50% demonstrates that $SO_2$ desorption is exergonic at typical SOFC operating temperatures. Removal of an initial 25% of atomic surface sulfur is considerably energetically favorable (50% → 25%, $\Delta G = -32.2$ kcal/mol). While the corresponding reaction concerning the removal of the remaining 25% sulfur is still favorable (25% → 0%, $\Delta G = -7.2$ kcal/mol), the resulting rate of $SO_2$ desorption for the latter reaction will be considerably smaller at 800 °C. This difference in activity when comparing the energetics of the reaction mechanisms corresponding to initial sulfur coverage of 50 and 25%, respectively, is due mainly to substantial steric interactions generated by the close proximity of neighboring atoms on the close-packed 50% sulfur (2S + 2O) surface. We have demonstrated that these steric interactions facilitates the immediate formation of $*SO_2$ and the subsequent formation of $SO_2$(g).

A CSTR kinetic model simulations allow further insight into the previously described reactions taking place on an initial atomic sulfur surface coverage of 50%. Occurring in a two-step process, the first step consists of the adsorption of $O_2$ followed by the immediate desorption of $SO_2$, removing approximately 20% of elemental surface sulfur and forming a small concentration of "clean" surface. At this stage the dominant $O_2/SO_2$ adsorption/desorption reaction mechanism involves an initial atomic sulfur surface coverage of 50%. Subsequent $O_2$ adsorptions on the newly formed 25% sulfur surface, the second step in the process, results in the formation and surface build-up of the stable species *SO–*O1. However, due to the large reactant concentration (*S–*S) remaining, this species in-turn associates, forms $SO_2$ and is swiftly desorbed, resulting in the complete elimination of all sulfur-based surface species. Based on data gathered from the CSTR model, we can deduce that the large $O_2$ adsorption energy barriers are not detrimental to the overall reaction.

Furthermore, while the intermediate species $^{*}SO$–$^{*}O1$ is almost as energetically stable as the overall product (clean surface + $SO_2(g)$) and the product itself is only slightly exergonic in nature, complete removal of atomic sulfur via $SO_2$ desorption will occur at 800 °C. Further DFT studies considered the formation and removal of elemental sulfur ($S_2$), with and without the presence of atomic oxygen. However, due to substantial energy barriers, the removal of $S_2(g)$ is unlikely to occur under these conditions as $SO_2$ desorption is energetically more favorable.

Based on the Gibbs' free energy reaction profile and the corresponding CSTR kinetic model, our research at temperature >800 °C has demonstrated the ease with which atomic sulfur can be removed from the surface as $SO_2$, after the adsorption of molecular oxygen, up to an initial elemental sulfur coverage of 50%. Based on this data, the production of $SO_2(g)$ is a viable method to regain electrochemical activity lost due to SOFC anode sulfur poisoning.

## Acknowledgments

Financial support was provided by the Alberta Energy Research Institute and the Western Economic Diversification Department. All calculations were carried out on WestGrid computing resources, funded in part by the Canada Foundation for Innovation, Alberta Innovation and Science, BC Advanced Education, and the participating research institutions. The WestGrid equipment was provided by IBM, Hewlett Packard, and SGI.

## Supplementary information

Derivations of rate expression for individual species and calculated reaction rate constants within kinetic profile.

Please visit DOI: 10.1016/j.jcat.2009.03.001.

## References

[1] R.M. Ormerod, Chem. Soc. Rev. 32 (2003) 17.
[2] S. McIntosh, R.J. Gorte, Chem. Rev. 104 (2004) 4845.
[3] M.C. Williams, J.P. Strakey, W.A. Surdoval, L.C. Wilson, Solid State Ionics 177 (2006) 2039.
[4] C.H. Bartholomew, P.K. Agrawal, J.R. Katzer, Adv. Catal. 31 (1982) 135.
[5] Y. Matsuzaki, I. Yasuda, Solid State Ionics 132 (2000) 261.
[6] M. Gong, X. Liu, J. Trembly, C. Johnson, J. Power Sources 168 (2007) 289.
[7] S. Hui, A. Petric, J. Eur. Ceram. Soc. 22 (2002) 163.
[8] P.R. Slater, D.P. Fagg, J.T.S. Irvine, J. Mater. Chem. 7 (1997) 2495.
[9] B.D. Madsen, S.A. Barnett, Solid State Ionics 176 (2005) 2545.
[10] Y.H. Huang, R.I. Dass, Z.L. Xing, J.B. Goodenough, Science 312 (2006) 254.
[11] S. Park, J.M. Vohs, R.J. Gorte, Nature 404 (2000) 265.
[12] S.C. Singhal, R.J. Ruka, J.E. Bauerle, C.J. Spengler, Anode development for solid oxide fuel cells, Final Technical Report, DOE/MC/22046-2371, U.S. Department of Energy, Washington, DC. 1986.
[13] K. Sasaki, K. Susuki, A. Iyoshi, M. Uchimura, N. Imamura, H. Kusaba, Y. Teraoka, H. Fuchino, K. Tsujimoto, Y. Uchida, N. Jingo, in: S.C. Singhal, J. Mizusaki (Eds.), Solid Oxide Fuel Cells IX, PV 2005-07, in: The Electrochem. Soc. Proc. Ser., The Electrochem. Soc., Pennington, NJ, 2005, p. 1267.
[14] S.J. Xia, V.I. Birss, in: S.C. Singhal, J. Mizusaki (Eds.), Solid Oxide Fuel Cells IX, PV 2005-07, in: The Electrochem. Soc. Proc. Ser., The Electrochem. Soc., Pennington, NJ, 2005, p. 1275.
[15] J.R. Rostrup-Nielsen, J.B. Hansen, S. Helveg, N. Christiansen, A.K. Jannasch, Appl. Phys. A 85 (2006) 427.
[16] K. Sasaki, K. Susuki, A. Iyoshi, M. Uchimura, N. Imamura, H. Kusaba, Y. Teraoka, H. Fuchino, K. Tsujimoto, Y. Uchida, N. Jingo, J. Electrochem. Soc. 153 (2006) A2023.
[17] S. Zha, Z. Cheng, M. Liu, J. Electrochem. Soc. 154 (2007) B201.
[18] Z. Cheng, M. Liu, Solid State Ionics 178 (2007) 925.
[19] J.B. Hansen, Electrochem. Solid State Lett. 11 (2008) B178.
[20] J.H. Wang, M. Liu, J. Power Sources 176 (2008) 23.
[21] J.N. Kuhn, N. Lakshminarayanan, U.S. Ozkan, J. Mol. Catal. A Gen. 282 (2008) 9.
[22] Y.S. Ku, S.H. Overbury, Surf. Sci. 276 (1992) 262.
[23] N.M. Galea, E.S. Kadantsev, T. Ziegler, J. Phys. Chem. C 111 (2007) 14457.
[24] P.H. Holloway, J.B. Hudson, Surf. Sci. 33 (1972) 56.
[25] H. Windawi, J.R. Katzer, J. Vac. Sci. Technol. 16 (1979) 497.
[26] Y. Zeng, S. Kaytakoglu, D.P. Harrison, Chem. Eng. Sci. 55 (2000) 4893.
[27] G. Kresse, J. Hafner, Phys. Rev. B 47 (1993) 558.
[28] G. Kresse, J. Furthmüller, Comput. Mat. Sci. 6 (1996) 15.
[29] G. Kresse, J. Furthmüller, Phys. Rev. B 54 (1996) 11169.
[30] P.E. Blöchl, Phys. Rev. B 50 (1994) 17953.
[31] G. Kresse, D. Joubert, Phys. Rev. B 59 (1999) 1758.
[32] J.P. Perdew, K. Burke, M. Ernzerhof, Phys. Rev. Lett. 77 (1996) 3865.
[33] H.J. Monkhorst, J.D. Pack, Phys. Rev. B 13 (1976) 5188.
[34] P. Villars, L.D. Calvert, Pearson's Handbook of Crystallographic Data for Intermetallic Phases, Am. Soc. Metals, Metal Park, OH, 1985.
[35] H. Jónsson, G. Mills, K.W. Jacobsen, in: B.J. Berne, G. Ciccotti, D.F. Coker (Eds.), Classical and Quantum Dynamics in Condensed Matter Phase Simulations, World Scientific, Singapore, 1998, p. 385.
[36] M.Y. Sun, A.E. Nelson, J. Adjaye, Catal. Lett. 109 (2006) 133.
[37] MatLab software (Version 6.5.1 Release 13, Service Pack 1), http://www.mathworks.com.
[38] T. Ohta, T. Yokoyama, S. Terada, A. Imanishi, Y. Kitajima, Res. Chem. Intermed. 26 (2000) 29.
[39] A. Galtayries, C. Cousi, S. Zanna, P. Marcus, Surf. Interface Anal. 36 (2004) 997.
[40] G.J. Jackson, D.P. Woodruff, A.S.Y. Chan, R.G. Jones, B.C.C. Cowie, Surf. Sci. 577 (2005) 31.
[41] J. Yoshinobu, X. Guo, J.T. Yates, J. Chem. Phys. 92 (1990) 7700.
[42] T. Edmonds, J.J. McCarroll, R.C. Pitkethly, J. Vac. Sci. Technol. 8 (1971) 68.
[43] Y. Kitajima, T. Yokoyama, T. Ohta, M. Funabashi, N. Kosugi, H. Kuroda, Surf. Sci. 214 (1989) L261.
[44] D.P. Woodruff, Phys. Rev. Lett. 72 (1994) 2499.
[45] A.R. Kortan, R.L. Pack, Phys. Rev. B 23 (1981) 6340.
[46] A. Eichler, F. Mittendorfer, J. Hafner, Phys. Rev. B 62 (2000) 4744.
[47] T. Yokoyama, S. Terada, S. Yagi, A. Imanishi, S. Takenaka, Y. Kitajima, T. Ohta, Surf. Sci. 324 (1995) 25.
[48] S. Cao, J.-C. Tang, P. Zhu, L. Wang, J. Phys. Condens. Matter 13 (2001) 5865.
[49] Y. Sakai, M. Koyanagi, K. Mogi, E. Miyoshi, Surf. Sci. 513 (2002) 272.
[50] G.J. Jackson, J. Lüdecke, S.M. Driver, D.P. Woodruff, R.G. Jones, A. Chan, B.C.C. Cowie, Surf. Sci. 389 (1997) 223.
[51] T. Smith, Ph.D. thesis, University of Calgary, Calgary, Canada, 2007.
[52] P. Zebisch, M. Weinelt, H.-P. Steinrück, Surf. Sci. 295 (1993) 295.